

Reconstructing the cosmological density and velocity fields from redshifted galaxy distributions using V-net

Fei Qin,^{a,1} David Parkinson,^{a,b} Sungwook E. Hong,^{a,b} Cristiano G. Sabiu.^c

^aKorea Astronomy and Space Science Institute,
776 Daedeok-daero, Yuseong-gu, Daejeon 34055, Republic of Korea

^bAstronomy Campus, University of Science and Technology,
776 Daedeok-daero, Yuseong-gu, Daejeon 34055, Republic of Korea

^cNatural Science Research Institute, University of Seoul,
163 Seoulsiripdaero, Dongdaemun-gu, Seoul 02504, Republic of Korea

E-mail: feiqin@kasi.re.kr, davidparkinson@kasi.re.kr, swhong@kasi.re.kr,
csabiu@uos.ac.kr

Abstract.

The distribution of matter that is measured through galaxy redshift and peculiar velocity surveys can be harnessed to learn about the physics of dark matter, dark energy, and the nature of gravity. To improve our understanding of the matter of the Universe, we can reconstruct the full density and velocity fields from the galaxies that act as tracer particles. We use a convolutional neural network, a V-net, trained on numerical simulations of structure formation to reconstruct the density and velocity fields. We find that, with detailed tuning of the loss function, the V-net could produce better fits to the density field in the high-density and low-density regions, and improved predictions for the amplitudes of the velocities. We also find that the redshift-space distortions of the galaxy catalogue do not significantly contaminate the reconstructed real-space density and velocity field. We estimate the velocity field β parameter by comparing the peculiar velocities of mock galaxy catalogues to the reconstructed velocity fields, and find the estimated β values agree with the fiducial value at the 68% confidence level.

¹Corresponding author.

Contents

1	Introduction	1
2	Creating the mock data	2
2.1	Particle simulations	2
2.2	Training and testing data sets	4
2.3	Galaxy peculiar velocity catalogues	5
3	Machine learning architecture: V-net	6
4	Reconstructing the density and velocity fields	8
4.1	Reconstructing the density field from the galaxy catalogue	8
4.2	Reconstructing the velocity field from the reconstructed density field	11
5	Estimating the β parameter	14
6	Conclusion	17

1 Introduction

Observations of the Universe suggest that it is mostly composed of a mysterious dark matter, in addition to galaxies, and that the expansion is currently being accelerated by the mysterious dark energy. Understanding the nature of dark matter and dark energy is crucial for us to comprehend the evolution of the Universe. This is also one of the key science goals of next-generation surveys, such as the Dark Energy Spectroscopic Instrument (DESI) [13], Euclid [50], the Widefield ASKAP L-band Legacy All-sky Blind Survey (WALLABY) [32], the Square Kilometre Array (SKA) [65], and the Legacy Survey of Space and Time (LSST) [29].

However, observations of the Universe only provide us with information about galaxies, as non-luminous baryonic matter and dark matter are not directly detectable by telescopes. A commonly used method for leveraging this information to improve our understanding of the total matter in the Universe is the reconstruction of the matter density and velocity fields using galaxy surveys, in which galaxies trace the underlying matter distribution of the Universe.

Peculiar velocities, which arise from the gravitational effects of matter density fluctuations, are good indicators of the matter density field in the nearby Universe. In linear perturbation theory, the relation between the peculiar velocity field of matter and galaxy contrast field is given by [4, 8, 63, 64, 66]

$$\mathbf{V}(\mathbf{r}) = \frac{\beta}{4\pi} \int \frac{\mathbf{r}' - \mathbf{r}}{|\mathbf{r}' - \mathbf{r}|} \delta_g(\mathbf{r}') d\mathbf{r}', \quad (1.1)$$

with the velocity-density coupling parameter β predicted to be

$$\beta = \frac{f}{b}. \quad (1.2)$$

Here, $b \equiv \delta_g/\delta$ is the biasing parameter, defined as the ratio between the galaxy contrast field δ_g and matter density contrast field δ . $f(\Omega_m)$ is the growth rate of the large scale structure, $f = d \ln \delta / d \ln a$, which is related to the matter density in standard Einstein gravity through the standard relation

$$f = \Omega_m(z)^{0.545}. \quad (1.3)$$

The parameter β can be estimated using the so-called velocity-velocity comparison method, i.e. comparing the measured peculiar velocities to the (peculiar) velocity field reconstructed from the real-space density field, while this density field is reconstructed from the redshift-space galaxy catalogues [4, 8, 15, 34, 36, 63, 63, 64, 66]. The measurement of β parameter enables us to constrain the cosmological models. Comparing to the galaxy correlation function and power spectrum measurements, the velocity-velocity comparison is a much more accurate method to derive β since it is almost free from cosmic variance [8, 34, 53, 59]. Particularly, if the peculiar velocities measured from the Type Ia supernovae samples are used to compare to the reconstructions [4, 8], this method will give an extraordinary accurate estimation of β , especially when the supernovae are too sparse to calculate the correlation functions and power spectrum very precisely.

In previous works [3, 5, 6, 8, 11, 16, 31, 33, 47, 70, 72], the reconstruction of the velocity field from the density field is based on their relationship described by linear theory. However, this method does not well predict the velocity field around very dense regions, mainly due to complex nonlinear effects [71]. Recently, artificial intelligence (AI) technology has been introduced into cosmology [7, 35, 38, 46, 56, & references therein]. Particularly, the utilization of the convolutional neural networks (CNN) for the density and velocity fields reconstruction [17, 19, 21, 37, 40, 48, 71, 73] becomes a promising toolkit in the study of the large-scale-structure (LSS) of the Universe.

In this paper, we will use simulations to test a novel CNN architecture, the V-net [39], for reconstructing the real-space density fields from the galaxy catalogues of redshift-space, and reconstructing the velocity fields from the density fields. We will also estimate the β parameter by comparing the reconstructed velocity fields to the (simulated) galaxy peculiar velocity catalogues, in order to explore whether a reasonable cosmological constraint can be obtained from the AI-predicted density and velocity fields.

The paper is structured as follows. In Section 2, we introduce the simulation and the training data set, as well as the testing data set. In Section 3, we introduce the architecture of V-net. In Section 4, we explore the density and velocity fields reconstruction. In Section 5, we measure the β parameter. A conclusion is presented in Section 6.

2 Creating the mock data

2.1 Particle simulations

We generated our mock catalogues and density and velocity fields using PINOCCHIO (the PINpointing Orbit Crossing Collapsed Hierarchical Objects code, [9, 41–45, 57, 67]). PINOCCHIO is a semi-analytical algorithm that simulates structure formation through Lagrangian perturbation theory and ellipsoidal collapse, rather than a full N -body particle evolution approach used in codes such as GADGET [61, 62]. This approach does not track the full evolution of particles on an individual basis, but rather traces perturbations on different scales through a grid approach and identifies haloes from ellipsoidal collapse. This approach provides a massive speed-up in CPU time, allowing us to generate a large number of training sets very quickly.

To run the simulations, we chose values of the cosmological parameters given in Tab. 1, which are taken from the maximum likelihood values estimated by the 9-year Wilkinson Microwave Anisotropy Probe (WMAP9) from [20]. We assume a geometrically flat ($\Omega_k = 0$) Λ CDM cosmology with the dark energy equation of state fixed to the cosmological constant value $w = -1$ and standard cold dark matter.

The initial simulations are run with a cubic periodic box of side $L = 500h^{-1}\text{Mpc}$, each containing 512^3 dark matter particles. This gives a particle mass of $6.4 \times 10^{10}h^{-1}\text{M}_\odot$. We set a minimum halo member particle number of 10, meaning the minimum halo mass is $6.4 \times 10^{11}h^{-1}\text{M}_\odot$. We generated

Parameter	Symbol	Value
Matter density	Ω_m	0.25
Cosmological constant density	Ω_Λ	0.75
Baryon density	Ω_b	0.044
Hubble parameter	H_0	70 km/s/Mpc
Amplitude of fluctuations on scales of $8h^{-1}\text{Mpc}$	σ_8	0.8
Spectral index of perturbation	n_s	0.96

Table 1. The values of the cosmological parameters used for the PINOCCHIO simulations.

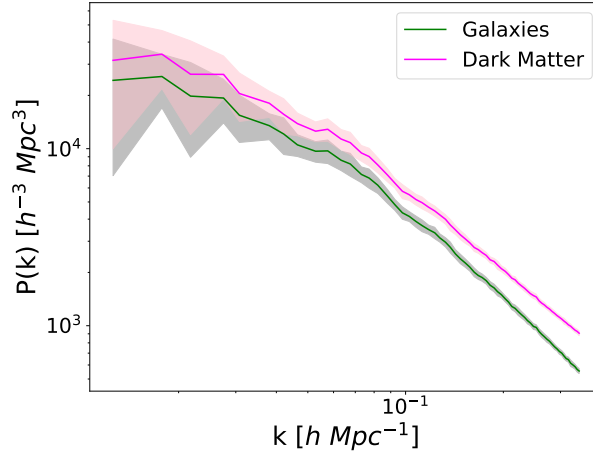


Figure 1. The density power spectrum of the simulations, measured in real space. The magenta curve is the average of the density power spectra of the dark matter of 42 simulation boxes. The pink area indicates the standard deviation of the 42 measurements. The green curve is the average of the density power spectra of the galaxies of the 42 simulation boxes. The grey area indicates the standard deviation of the 42 measurements.

a set of 42 simulations, each with a different initial condition defined by a change in the random seed. This change in initial condition was the only difference between the boxes, as we generated simulations for only a single set of cosmological parameters for this training and test set. The real space power spectra for all of these 42 simulations is shown in Figure 1.

The output of each simulation is the position and velocity of the particles, and a halo catalogue with position and velocity of each halo. All simulation outputs are at redshift $z = 0$, and we do not consider higher redshift matter distributions or construct a light cone that would include the effect of redshift evolution of the density field. The halo catalogue is an automatic output of the PINOCCHIO code through the *fragmentation* algorithm, which mimics the hierarchical process of accretion of matter and merging of haloes [43]. In this work, we use the haloes as proxies for the galaxies that will be observed, but with no selection based on observability or mass. Each simulation contains roughly 540,000 haloes, giving an average number density of $4.3 \times 10^{-3} h^3 \text{Mpc}^{-3}$, which is fairly close to the number density of the Two Micron All-Sky Survey (2MASS) Redshift survey [26] (estimated to be $5.4 \times 10^{-3} h^3 \text{Mpc}^{-3}$). In Fig. 1, the amplitude of the galaxy (halo) power spectrum is below that of the dark matter because the mean halo mass is small ($\sim 4.7 \times 10^{12} h^{-1} \text{M}_\odot$), leading to a galaxy bias less than unity [1, 54, 68].

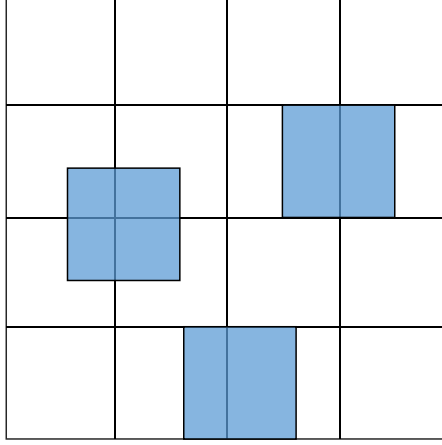


Figure 2. The data augmentation used in this work. We randomly choose 6850 sub-cubes (blue squares) which have overlap areas to the unattached 2,150 sub-cubes (white squares).

Dataset	Number
All sub-cubes	2,688
Testing set (no augmentation)	538
Sub-cubes (for training & validation) before augmentation	2,150
Sub-cubes (for training & validation) after augmentation	9,000
Training set (augmented)	7,200
Validation set (augmented)	1,800

Table 2. Number of sub-cubes of size $125 h^{-1}$ Mpc used in each stage of CNN training, validation and testing.

2.2 Training and testing data sets

To generate a large number of training cubes, each of the 42 large simulation boxes has been divided into 4^3 sub-cubes. The density and velocity field of each sub-cube is pixelised with 32^3 pixels. This pixel size is $\sim 4 h^{-1}$ Mpc, chosen as the best compromise to predict velocities from the smooth density fields which are compared to measured peculiar velocities [2, 4, 8, 64]. We finally have 2,688 sub-cubes, each with side length of $125 h^{-1}$ Mpc. Around 20% of these, i.e., 538 sub-cubes are randomly chosen as the testing data set.

We applied data augmentation to the remaining 80% of the sub-cubes to obtain 9,000 cubes as the training and validation data set. As illustrated in Fig. 2, we randomly choose 6,850 sub-cubes which have overlap areas to the unattached 2,150 sub-cubes. The minimum stride to both the unattached sub-cubes and other augmented sub-cubes is 8 pixels to avoid complete overlaps. Among these 9,000 sub-cubes, 20% are used to validate CNN. The number of each type and at each stage of preprocessing is given in Table 2.

The density (contrast) field is defined as:

$$\delta(\mathbf{r}) = \frac{\rho(\mathbf{r}) - \bar{\rho}}{\bar{\rho}} \quad (2.1)$$

where $\rho(\mathbf{r})$ is the mass density at real-space position \mathbf{r} , $\bar{\rho}$ is the average mass density of the Universe. The cloud-in-cell (CIC) algorithm¹ is adopted to the dark matter particles to obtain the density field

¹We use the PYTHON package NBODYKIT <https://github.com/bccp/nbodykit-cookbook/blob/master/>

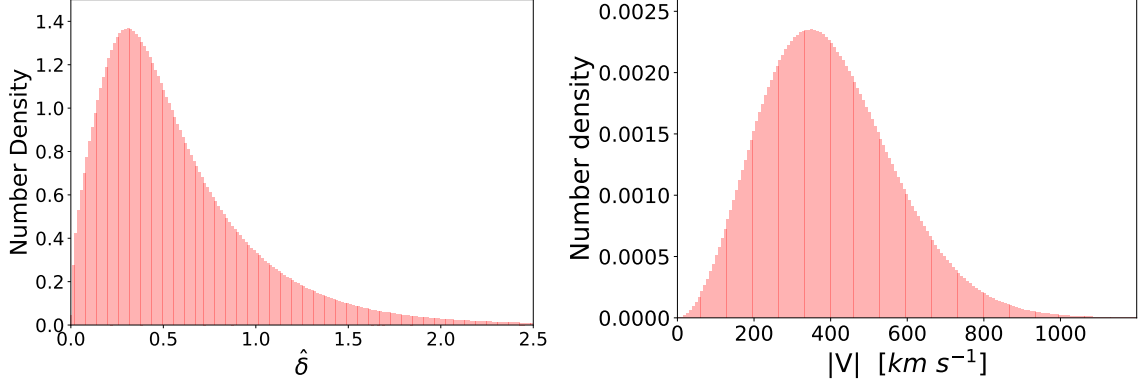


Figure 3. Probability distributions of normalized density $\hat{\delta}$ (left) and the velocity magnitude V (right) in our simulation.

cubes. The density values vary over three orders of magnitude, and so we renormalize the density field using

$$\hat{\delta} = \ln(1 + \rho/\bar{\rho}) \quad (2.2)$$

to reduce the variance.

For the velocity field cubes, the velocities of each pixel is simply calculated by averaging over the velocities of the particles in each pixel. We renormalize the velocity field using

$$\mathbf{u}(\mathbf{r}) = \frac{\mathbf{V}(\mathbf{r})}{\sigma_v} \quad (2.3)$$

so that the velocities will have the similar order of magnitude as the density values. $\sigma_v = 250 \text{ km s}^{-1}$ is the velocity dispersion (the standard deviation of the velocities) of our simulations. Fig. 3 shows the probability distributions of $\hat{\delta}$ and $V \equiv |\mathbf{V}|$ in our simulations.

The galaxy contrast field cubes are obtained using the same method as above, but this time using the halo catalogue instead of the dark matter particles. However, before this is done, 20% of the galaxies are separated out to create the peculiar velocity catalogue, which will be used only for estimating the β parameter in the final stage. To obtain the redshift-space galaxy contrast field, the redshift-space distortions (RSDs) have been added into the Z -direction using

$$Z_{\text{rsd}} = Z_{\text{real}} + \frac{1 + z_h}{H(z_h)} V_Z, \quad (2.4)$$

where Z_{rsd} and Z_{real} are the Z -direction coordinates of galaxies in redshift and real space, respectively. V_Z is the Z -direction component of the galaxy velocity. z_h is the cosmological redshift of our simulation snapshot² and $H(z_h)$ is the Hubble parameter.

2.3 Galaxy peculiar velocity catalogues

Once we obtain the reconstructed *real-space* density and velocity fields from the redshift-space galaxy contrast field, we can compare the reconstructions to the measured peculiar velocities to estimate the cosmological parameter β . In observations, the measured peculiar velocity values are mainly obtained

[recipes/painting.ipynb](#).

²If using a simulation of lightcone, z_h is the redshift of each galaxy.

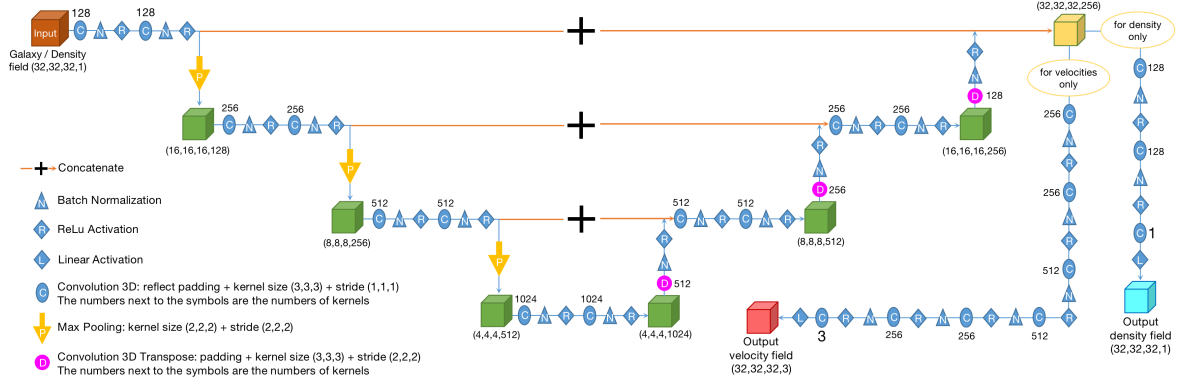


Figure 4. The V-net architecture used to reconstruct the density and velocity fields in this work .

from galaxies using the Tully-Fisher relation [24, 69] or Fundamental Plane [14, 25]. Therefore, it is necessary to generate mock galaxy peculiar velocity catalogues in order to estimate β in this paper.

The estimation of β is a separate task regardless of the RSDs and cosmological redshift of the galaxy mock catalogues mentioned in Section 2.2. Therefore, to build the mock galaxy peculiar velocity catalogues, we can assign cosmological redshifts z_h to the galaxies based on their real-space distances r , although these galaxies are sub-sampled from the galaxy catalogues of the snapshots corresponding to cosmological redshift zero. The line-of-sight peculiar velocity of a galaxy is calculated using

$$s_g = \mathbf{V}_g \cdot \hat{\mathbf{r}}, \quad (2.5)$$

where \mathbf{V}_g is the velocity of galaxies known from the simulations. $\hat{\mathbf{r}}$ is the unit vector corresponding to the real-space position \mathbf{r} , rather than setting the Z-direction as the line-of-sight. Then, the observed redshift of a galaxy is given by [10, 12, 27, 52, 55, 60]

$$1 + z_{\text{obs}} = (1 + z_h) \left(1 + \frac{s_g}{c} \right), \quad (2.6)$$

where c is the speed of light. The z_{obs} values will be used to estimate β in Section 5.

3 Machine learning architecture: V-net

The machine learning U-net architecture was initially proposed by [58]. Overall, this method has a similar architecture to the convolutional autoencoder (CAE). Both U-net and CAE consist of two stages — first, the encoding stage extracts features from the original image by increasing the number of channels and decreasing the image size of each channel. Then follows the decoding stage, which reconstructs the new image by decreasing the number of channels and increasing the image size of each channel. In addition to CAE, U-net uses concatenating both the outputs from the encoding stage and inputs from the decoding stage to convolve the outputs at the decoding stage, which prevents the loss of small-scale features in the CAE.

Recently, a three-dimensional extension of U-net, referred to as V-net, was proposed by [39]. The implementation of V-net has been utilized in the reconstruction of LSS in various studies, including [21, 71, 73]. The present study employs a CNN architecture, as depicted in Fig. 4, which is based on the original V-net framework with modifications inspired by the works of [21, 71].

Regarding the density field reconstruction, the redshift-space galaxy contrast fields are set to be the inputs of the CNN architecture. The real-space density fields are set to be the outputs of the

architecture. Each input galaxy contrast field has spatial dimension 32^3 and one channel, i.e., it has a shape of (32, 32, 32, 1).

1. First, they are fed into two convolution layers. Each convolution layer is designed to have 128 convolution kernels with a shape of 3^3 and a scanning stride of 1. Also, the reflect padding, which adds the padding pixels to the boundaries by mirror-reflecting the inner pixels, is applied to ensure that the outputs have the same dimension as the inputs, as well as to minimize the loss of information around the boundaries. A batch normalization [28] and a rectified linear unit (ReLU, [18]) activation function are used following each convolution layer. The final outputs of this step are a set of feature fields, and each feature field has a shape of (32, 32, 32, 128).
2. Then, these feature fields are fed into a max-pooling layer with a shape of 2^3 and 2-stride. Only the maximum values from nearby 2^3 pixels pass through the max-pooling layer, and the dimension of each feature field has been reduced to (16, 16, 16, 128) in this step.
3. For further feature extraction and compression, the outputs of the above step are processed by the same operations as steps 1–2 three more times. However, the number of convolution kernels used in each operation are changed to 256, 512, and 1024, and there is no max-pooling used in the third operation, as shown in the Fig. 4. The final output of this step has a shape of (4, 4, 4, 1024).
4. Then, they are fed into a de-convolution (or transpose convolution) layer. This layer is designed to have a padding and 512 de-convolution kernels. Each de-convolution kernel has a shape of 3^3 and the scanning stride is 2. A batch normalization and a ReLU activation function are applied. The final output has a shape of (8, 8, 8, 512).
5. The outputs of the above ‘decoding’ step will be concatenated with the feature fields of the equivalent (with a size of (8, 8, 8, 512)) ‘encoding’ stage. Then they will be fed into two convolution layers which are the same as Step 1, but using 512 convolution kernels.
6. The outputs of the above step are processed using the same operations as Steps 4–5 twice, but using 256 and 128 kernels, respectively. There is no convolution layer used in the last operation. The final output of this step has a shape of (32, 32, 32, 256).
7. To obtain the reconstructed density field, the feature fields are further processed by two convolution layers of 128 kernels. The kernel has a shape of 3^3 and 1-stride. The padding, batch normalization and ReLU activation function are applied to the outputs of each convolution layer too. The final convolution layer has only one kernel and followed by a ReLU activation function. The shape of the convolution kernel is 3^3 and the stride is 1.
8. Finally, we obtain the density field reconstructed from the galaxy catalogues. To reconstruct the velocity field, the reconstructed density fields (rather than the galaxy contrast fields) are set to be the inputs of the CNN architecture. Each density field has a shape of (32, 32, 32, 1) too. Correspondingly, the outputs of Step 6 will be processed by six convolution layers. The numbers of kernels used in the layers are listed in Fig. 4. The final convolution layer has three kernels and followed by a linear activation function. The shape of each convolution kernel is 3^3 and the stride is 1.

We implement the `TENSORFLOW`³ package to build the above architecture. The optimization method is the Adam algorithm [30]. The mini-batch size is 32. We stop training if the validation loss reaches its minimum and tend to be flat.

4 Reconstructing the density and velocity fields

4.1 Reconstructing the density field from the galaxy catalogue

We use the 9,000 training/validation galaxy cubes in redshift space and the density field cubes in real space as the inputs and outputs, respectively, in order to train the CNN. The trained V-net, corresponding to the minimum validation loss, is then applied to the 538 testing galaxy cubes to obtain the reconstructed density fields of the real space. We define the loss function as

$$\mathcal{L}_{\hat{\delta}} = \frac{1}{N_{\text{pix}}} \sum_{i=1}^{N_{\text{pix}}} \left(w_{\hat{\delta},i} |\hat{\delta}_{p,i} - \hat{\delta}_{t,i}| \right), \quad (4.1)$$

where $\hat{\delta}_{p,i}$, $\hat{\delta}_{t,i}$, and $w_{\hat{\delta},i}$ are the prediction and true values of the normalize density, and the weight factor for the i -th pixel, respectively.

The lack of a weight factor $w_{\hat{\delta},i}$ results in an inability for the V-net to accurately reproduce the density field in both high and low density regions. This is likely caused by the imbalanced training data, where the model may overfit to the most frequently occurring class with $\hat{\delta} \sim 0.3$ ($\rho \sim \bar{\rho}$), leading to poor performance on under-represented classes in both extremely dense and underdense regions (see the left panel of Fig. 3). Therefore, the inclusion of weight factors is crucial for improving predictions in both high and low density regions by adjusting for the imbalance in the training data.

For matching the distribution of the reconstructed density values δ_p to the true density values δ_t , we first decompose the density field into five regions as shown in Fig. 5: void centers ($\hat{\delta}_t \leq 0.1$; $\rho \leq 0.1\bar{\rho}$; top-middle), void boundaries ($0.1 < \hat{\delta}_t \leq 0.4$; $0.1 < \rho/\bar{\rho} \leq 0.5$; top-right), filaments ($0.4 < \hat{\delta}_t \leq 1$; $0.5 < \rho/\bar{\rho} \leq 1.7$; bottom-left), cluster outskirts ($1 < \hat{\delta}_t \leq 1.8$; $1.7 < \rho/\bar{\rho} \leq 5$; bottom-middle), and cluster centers ($\hat{\delta}_t > 1.8$; $\rho > 5\bar{\rho}$; bottom-right). Then we find the optimal choice of the weight function at each of aforementioned five regions,

$$w_{\hat{\delta},i} = \begin{cases} 1.3, & 0 < \hat{\delta}_{t,i} \leq 0.1 \\ 0.7, & 0.1 < \hat{\delta}_{t,i} \leq 0.4 \\ 1.2\hat{\delta}_{t,i} + 0.5, & 0.4 < \hat{\delta}_{t,i} \leq 1 \\ 2.3, & 1 < \hat{\delta}_{t,i} \leq 1.8 \\ 0.8\hat{\delta}_{t,i}^3 - 2.3656, & \hat{\delta}_{t,i} > 1.8 \end{cases}, \quad (4.2)$$

as shown in the left-side panel of Fig. 6.

The blue curve in the middle panel of Fig. 6 shows the evolution of loss function as a function of learning rate of the Adam optimizer. If the learning rate is lower than 10^{-6} , the update of the parameters is too slow, which is presented as a flat slope of the blue curve. On the contrary, a too high learning rate ($> 2 \times 10^{-3}$) prevents finding a solution. Therefore, we choose the learning rate 6×10^{-5} for density field reconstruction. The right panel of Fig. 6 shows the training loss (blue curve) and validation loss (orange curve) with the learning rate 6×10^{-5} . Beyond epoch equal to 90, the validation loss tends to be flat, therefore, we stop training at epoch equal to 160.

³TENSORFLOW: <https://www.tensorflow.org/>

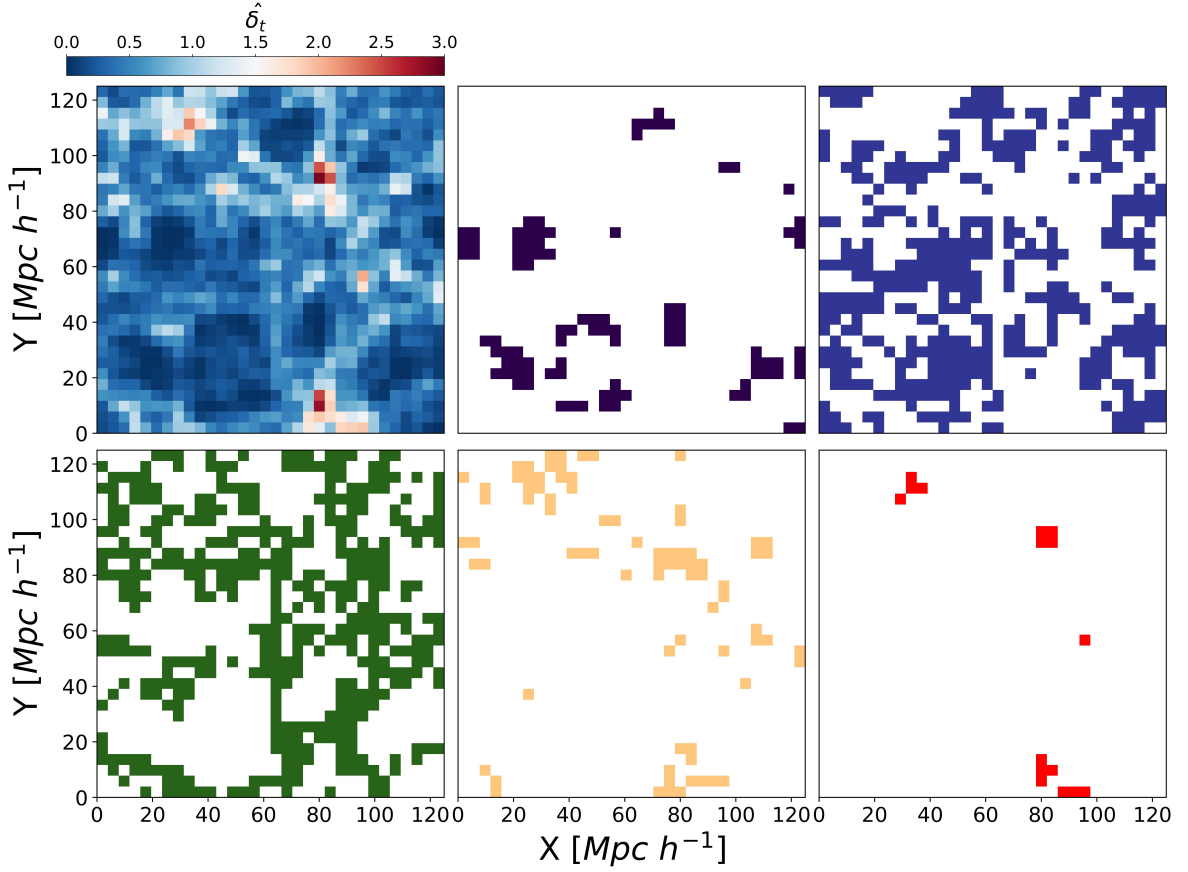


Figure 5. The decomposition of the density field. The top left panel shows an example slice of the true density field, the other panels show the decomposition of the slice. From top-middle to the bottom-right: void centers ($\rho \leq 0.1\bar{\rho}$), void boundaries ($0.1 < \rho/\bar{\rho} \leq 0.5$), filaments ($0.5 < \rho/\bar{\rho} \leq 1.7$), cluster outskirts ($1.7 < \rho/\bar{\rho} \leq 5$), and cluster centers ($\rho > 5\bar{\rho}$).

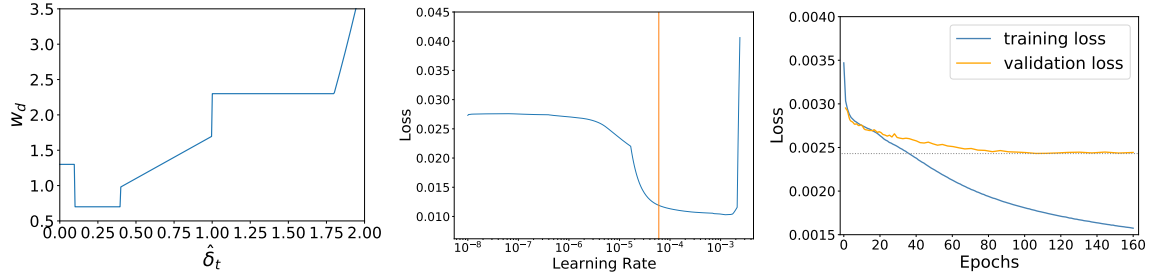


Figure 6. Left: Weights for reconstructing the density field, w_{δ} as a function of true density field. Middle: Evolution of loss function as a function of learning rate (blue curve) and the learning rate we have adopted (orange line). Right: Loss function of density field reconstruction as a function of training epoch.

Fig. 7 shows the comparison between the reconstructed density field images (top panels) and the true density field images (bottom panels) in the XY-, XZ- and YZ-planes. The V-net predictions of tiny and large filaments, as well as the voids, match the true fields with high fidelity. Also, the V-net gives reasonable predictions of the density fields with less contamination from the RSDs (applied to

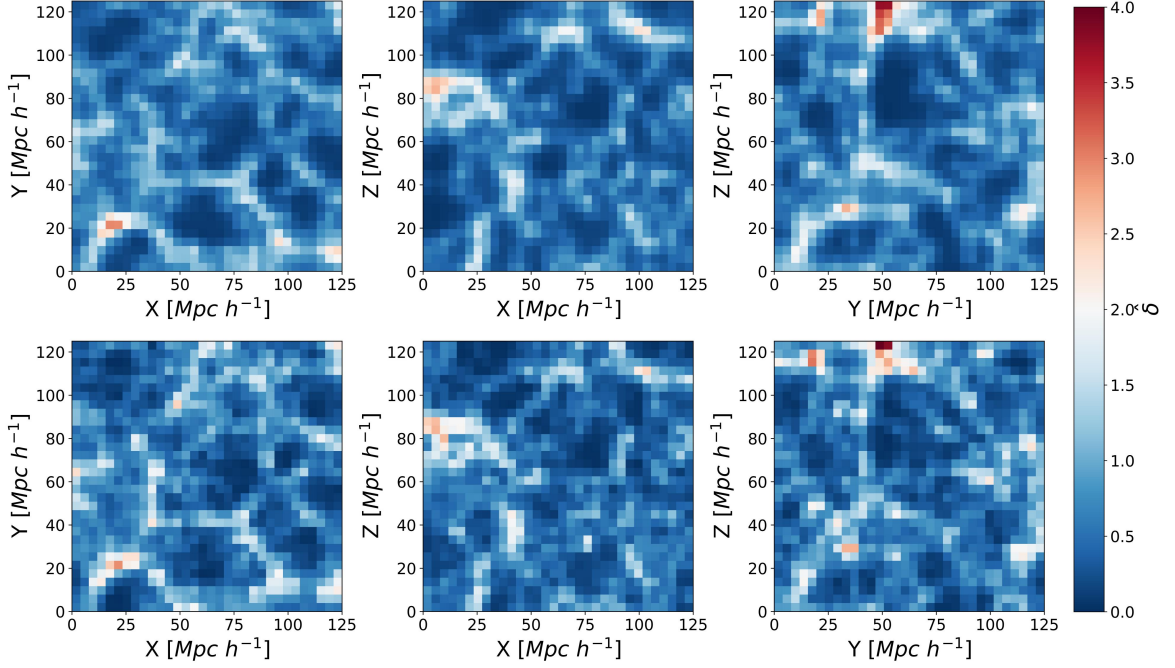


Figure 7. Comparison between the reconstructed density fields (top) and the true density fields (bottom) in XY-, XZ- and YZ-planes, respectively. The thickness of each slice is $4 h^{-1}$ Mpc (one pixel size).

the Z-direction) of the galaxy catalogues. Note that, however, the reconstructed filamentary structure is smoother and less complex than the true field, overall. Also, for some very massive clusters, our reconstruction exhibits somewhat different substructures than the true field (e.g., see YZ-plane with $(Y, Z) = (40 h^{-1} \text{Mpc}, 120 h^{-1} \text{Mpc})$). We suspect this may be partially due to the limitation of our halo sample, which has a similar number density to the 2MASS Redshift survey. Structures associated with much smaller scales than the scales allowed by our halo sample may not be reconstructed well even with our CNN method. Therefore, to marginalize such problems, one may need to try either adopting galaxy/halo samples with higher number density or making the spatial resolution of the density cube lower. We leave both possibilities as future works.

In the top-left panel of Fig. 8, the distributions of the reconstructed density values $\hat{\delta}_p$ of the 538 testing cubes is shown in green bars, while the corresponding true density values $\hat{\delta}_t$ is shown in pink bars. The fractional residual between $\hat{\delta}_p$ and $\hat{\delta}_t$ is mostly smaller than 1, as displayed in the top-right panel. Note that, however, our V-net reconstruction does not reconstruct the probability distribution of density in highly underdense regions $\hat{\delta} < 0.1$ (i.e., $\rho < 0.1\bar{\rho}$) well. While our changes of the weight factors could not remove such biases at the underdense pixels, these regions will not dominate the clustering and correlation function measurements, and therefore, the biases are negligible to constrain cosmology.

The bottom-left panel shows $\hat{\delta}_p$ against $\hat{\delta}_t$, with the white colored contours indicating the 68%, 95%, and 99.7% confidence levels. The reconstructed density values largely agree with the true density values. Note that there exist a small population with very high true density value and relatively low reconstructed value ($\hat{\delta}_p \lesssim 3 - 4 \lesssim \hat{\delta}_t$; $\rho_p \lesssim 10^{3-4} \bar{\rho} \lesssim \rho_t$), while there is no such population with very high reconstructed density value and relatively low true value ($\rho_t \lesssim 10^{3-4} \bar{\rho} \lesssim \rho_p$). This matches well with our observation in Fig. 8 that the reconstructed density field is somewhat smoother than the true density field.

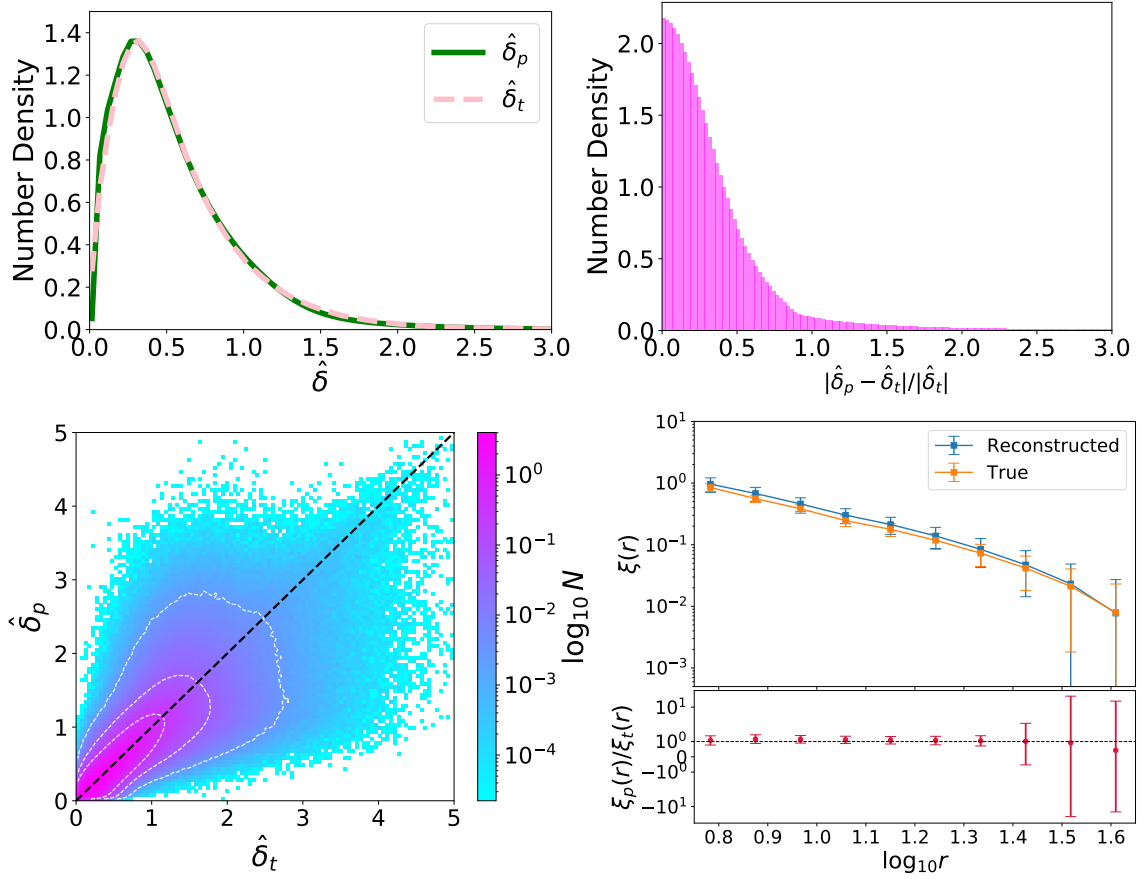


Figure 8. Top-left: Probability distributions of the reconstructed density values $\hat{\delta}_p$ (green solid curve) and true density values $\hat{\delta}_t$ (pink dashed curve) for 538 testing cubes, respectively. Top-right: Probability distribution of residual between the reconstructed and true density values for these cubes. Bottom-left: The reconstructed density values against the true values, with the white colored contours indicating the 68%, 95%, and 99.7% confidence levels. Bottom-right: Two-point correlation functions of the reconstructed (blue) and true (orange) density fields for the averaging of 538 testing cubes, respectively. The unit of r is $h^{-1}\text{Mpc}$.

In the bottom-right panel, the orange curve and the error bars are the average and the standard deviation of the two-point correlation function of the 538 true density fields, respectively, while the blue curve and the error bars are the average and the standard deviation of the correlation function of the 538 reconstructed density fields, respectively. As expected from the above analyses, both two-point correlation functions match well with each other within the error bar. The error bars of the orange colored curve represent the variance between the sub-cubes and the whole simulation box. i.e. cosmic variance. The error bars of the blue colored curve represent the cosmic variance combined with the errors caused by the CNN reconstruction.

4.2 Reconstructing the velocity field from the reconstructed density field

To reconstruct the velocity fields from the density fields, we first need to apply the V-net model trained from the above density field reconstruction to the 9,000 training galaxy contrast cubes to obtain 9,000 reconstructed density cubes. After that, we use these reconstructed density fields as the inputs to train the V-net. The V-net architecture for velocity reconstruction, which is slightly different from density field reconstruction, is presented in Section 3 and Fig. 4. The corresponding 9,000 true velocity field

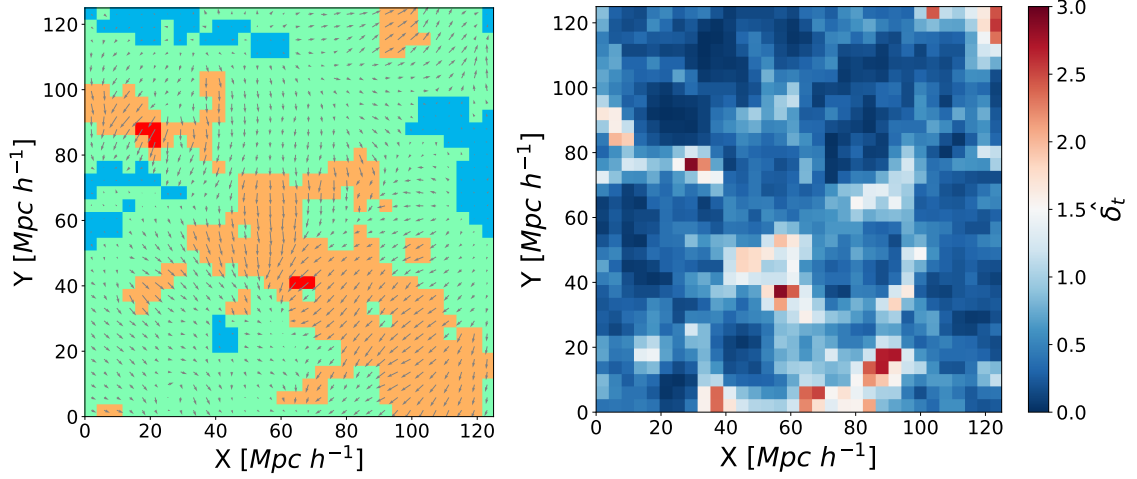


Figure 9. The left panel shows the decomposition of an example slice of the true velocity field. The blue colored pixels shows the velocities in the interval $V_t \leq 175 \text{ km s}^{-1}$, the green colored pixels shows the velocities in the interval $175 \text{ km s}^{-1} < V_t \leq 500 \text{ km s}^{-1}$, the orange colored pixels shows the velocities in the interval $500 \text{ km s}^{-1} < V_t \leq 750 \text{ km s}^{-1}$, and the red colored pixels shows the velocities in the interval $V_t > 750 \text{ km s}^{-1}$. The right panel shows the corresponding density field.

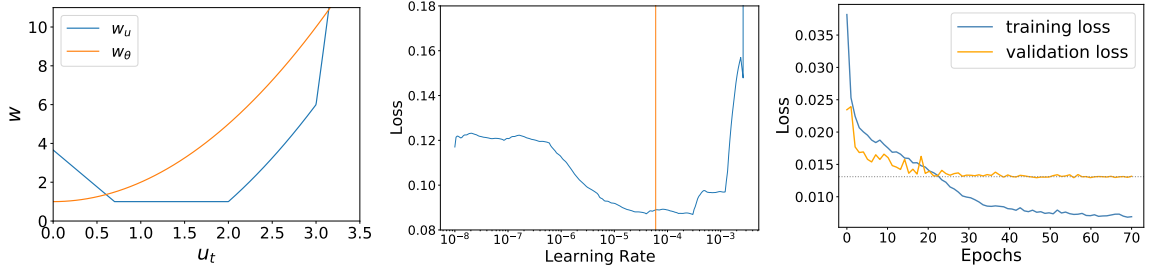


Figure 10. Left: Weights for reconstructing the velocity field, w_θ and w_u as functions of true density field. Middle: Evolution of loss function as a function of learning rate (blue curve) and the learning rate we have adopted (orange line). Right: Loss function of velocity field reconstruction as a function of training epoch.

cubes, normalized using Eq. 2.3, are set to be the outputs of the V-net for training. Then, the trained V-net with the minimum validation loss is applied to the 538 reconstructed test density fields to obtain the reconstructed test velocity fields. We define the loss function as:

$$\mathcal{L}_{u,\theta} = \mathcal{L}_u + \mathcal{L}_\theta = \frac{1}{N_{\text{pix}}} \sum_{i=1}^{N_{\text{pix}}} (w_{u,i} |u_{p,i} - u_{t,i}| + w_{\theta,i} |\cos \theta_i - 1|), \quad (4.3)$$

where $u = |\mathbf{u}|$ denotes the amplitude of the normalized velocity, $\cos \theta$ is the angle between the predicted velocity and true velocity, and w_θ and w_u are the weight factors for θ and u , respectively.

Similar to what we have found in Section 4.1, without introducing any specific weight factors w_θ and w_u , the machine learning would try to match only the most common population, which have $V \sim 400 \text{ km s}^{-1}$. As a result, we find that our method underestimates the velocities of both the larger and smaller amplitudes. Also, the directions of the velocities of larger amplitudes are not well predicted either. Therefore, similar to Section 4.1, the weight factors are required to reconstruct velocity fields with both large and small amplitudes well.

Similar to what we have done in the previous subsection, we decompose the true velocity field into four regions as shown in Fig. 9: low-velocity region around void centers ($u_t \leq 0.7$; $V_t \leq 175 \text{ km s}^{-1}$; blue), mid-velocity region ($0.7 < u_t \leq 2$; $175 \text{ km s}^{-1} < V_t \leq 500 \text{ km s}^{-1}$; green), high-velocity region around void boundaries and filaments ($2 < u_t \leq 3$; $500 \text{ km s}^{-1} < V_t \leq 750 \text{ km s}^{-1}$; orange), and very-high-velocity region around cluster outskirts ($u_t > 3$; $V_t > 750 \text{ km s}^{-1}$; red). We then find the optimal choice of the weight function for the velocity magnitude w_u to match the distribution of the reconstructed velocities V_p to the true V_t for each of the aforementioned four regions. In case of the weight function for the velocity angle w_θ , on the other hand, we do not apply the results of the velocity decomposition, mainly because the angular term in the loss function $\mathcal{L}_\theta \sim w_\theta |\cos \theta - 1|$ has little dependency on the velocity magnitude. Instead, we find the optimal choice of w_θ at the entire range of u_t , only assuming that the directional accuracy of velocity field is less important for velocities with lower magnitude.

By matching the distribution of the reconstructed velocities V_p to the true V_t from the 538 testing data sets, we find the optimal weighting schedule is:

$$w_{\theta,i} = u_{t,i}^2 + 1, \quad w_{u,i} = \begin{cases} -3.8u_{t,i} + 3.66, & 0 < u_{t,i} \leq 0.7 \\ 1, & 0.7 < u_{t,i} \leq 2 \\ u_{t,i}^2 - 3, & 2 < u_{t,i} \leq 3 \\ 5.5u_{t,i}^2 - 43.5, & u_{t,i} > 3 \end{cases} \quad (4.4)$$

see left panel of Fig. 10.

The middle panel of Fig. 10 shows the evolution of the loss function as a function of the learning rate of the Adam optimizer. Similar to Fig. 6, if the learning rate is lower than 10^{-6} , the update of the parameters is too slow, while a too high learning rate ($> 2 \times 10^{-3}$) prevents finding a solution. Therefore, we choose the learning rate 6×10^{-5} for velocity field reconstruction. The right panel shows the training loss (blue curve) and validation loss (orange curve) by adopting the above learning rate. The validation loss tends to be flat beyond epoch 30, and therefore, we stop training at epoch 70.

Fig. 11 shows the comparison between the reconstructed velocity field images (top panels) and true velocity field images (bottom panels) in the XY-, XZ-, and YZ-planes. Overall, both the amplitudes and directions of the V-net predicted velocity excellently match the true velocity, as well as the large-scale-structure features. Also, as seen from the velocity fields in the XZ- and YZ-planes (the middle and right panels), there is no significant RSD contamination in the reconstructed real-space velocity fields. Note that, however, there is a significant difference on the velocity fields, both in terms of magnitude and direction, at the interface between filaments and massive clusters (XZ-plane with $(X, Z) = (30 h^{-1} \text{Mpc}, 60 h^{-1} \text{Mpc})$). Even with the dark matter-only semi-analytic simulations, such regions might be highly nonlinear and associated with energetic infall shock waves [22, 23]. However, we expect that such local disagreement in nonlinear regions may not significantly affect our goal to estimate the β parameter, and we leave it as future works.

In the top-left panel of Fig. 12, the pink bars show the distribution of the true velocity amplitudes V_t , while the green bars shows the distribution of the reconstructed velocity amplitudes V_p , while the top-middle panel displays the fractional residuals between V_t and V_p , most of which are smaller than 1. The top-right panel shows the distribution of $\cos \theta$. In an ideal reconstruction, $\cos \theta$ should be one, and most of our reconstructions have the value close to one. Note that a small fraction of the population have even negative value of $\cos \theta$, and we suspect that most of them would have very small velocity amplitude (see the bottom panel, for example).

In the bottom panel, we plot the three components of the reconstructed velocities against the true velocities. The white colored contours indicate the 68%, 95%, and 99.7% confidence levels,

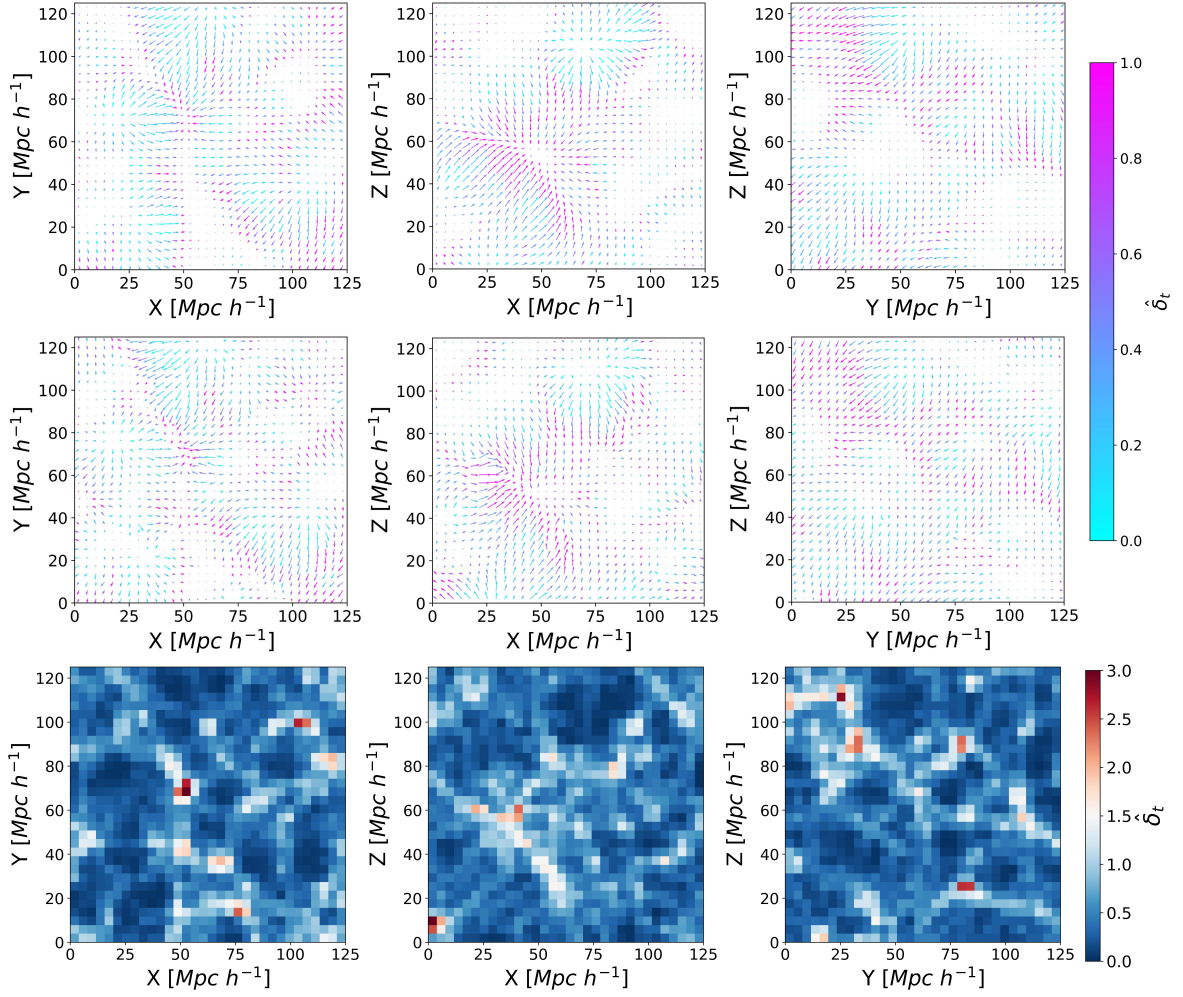


Figure 11. Comparison between the reconstructed velocity fields (top) and the true velocity fields (middle) in XY-, XZ- and YZ-planes, respectively. The thickness of each slice is $4 h^{-1} \text{ Mpc}$ (one pixel size). The bottom panels show the corresponding true density fields.

and the reconstructed velocity fields are largely agree with the true velocity fields. Interestingly, the distribution of true and reconstructed V_Z is similar to those of V_X and V_Y , indicating that our reconstruction does not suffer much of the RSD contamination.

5 Estimating the β parameter

Once we obtain the reconstructed real-space density and velocity fields, we can compare the reconstructions to the measured peculiar velocities to estimate the cosmological parameter β . Eq. 1.1 shows how the velocity field is coupled to the density field through the value of this parameter, which acts as a coupling coefficient. The reconstructed velocity V_p scales with the fiducial $\beta_{\text{fid}} = 0.52$ of the simulations, while the amplitudes of the measured peculiar velocities of galaxies V_g should scale with the measured β . Thus [63, 64],

$$\frac{V_g}{\beta} = \frac{V_p}{\beta_{\text{fid}}}, \quad (5.1)$$

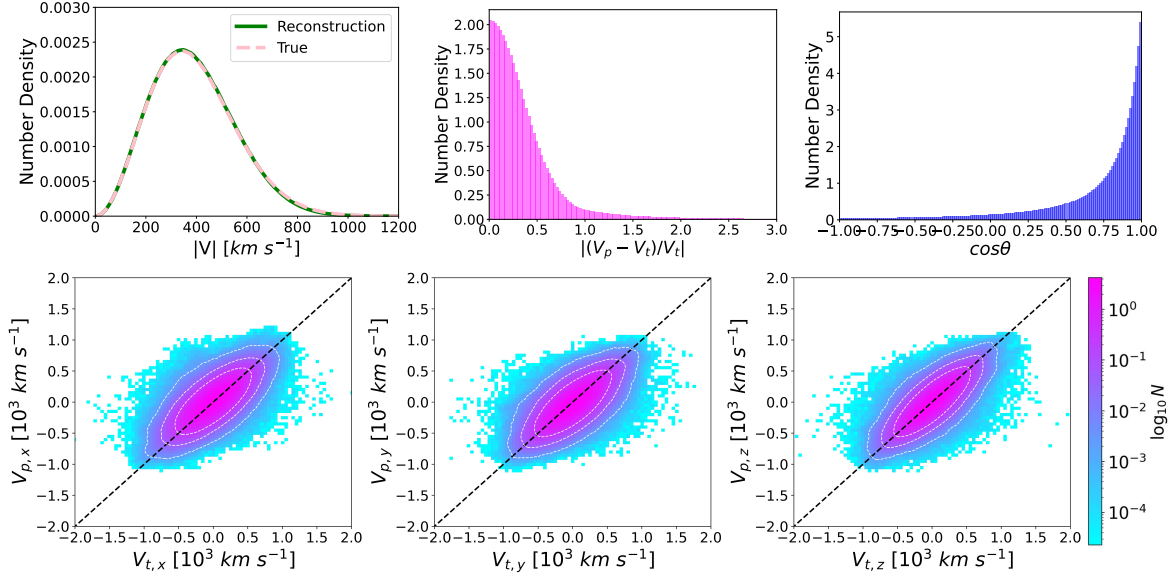


Figure 12. Top-left: Distributions of the true velocity amplitudes V_t (pink dashed curve) and the reconstructed velocity amplitudes V_p (green solid curve). Top-middle: Distribution of the fractional residuals between V_t and V_p . Top-right: The distribution of $\cos \theta$. Bottom: Comparisons between the three components of reconstructed velocities to their true velocity counterparts. The white colored contours indicate the 68%, 95%, and 99.7% confidence levels.

and therefore, to measure β , the reconstructed velocity fields should be divided by the fiducial β_{fid} .

In observations, the measurement errors of galaxy peculiar velocities are very large (typically around 20–25% error on distance estimates for Fundamental Plane and Tully-Fisher galaxies). To obtain a more accurate estimation of β , the measurement needs to be performed in terms of redshift [4, 8, 63, 64]. Therefore, to simulate the measurement procedure in real observations, we need to project the reconstructed velocity to the line-of-sight and re-scale to $\beta = 1$ using

$$s = \frac{1}{\beta_{\text{fid}}} \mathbf{V}_p \cdot \hat{\mathbf{r}}. \quad (5.2)$$

Then we can calculate the observed redshift z_p (of a galaxy at real-space position \mathbf{r}) predicted from our reconstructions using [4, 8]

$$1 + z_p = (1 + z_h) \left[1 + \frac{1}{c} (\beta s + \mathbf{V}_{\text{ext}} \cdot \hat{\mathbf{r}}) \right]. \quad (5.3)$$

The reconstruction is usually performed within a limited survey volume D , therefore a extra nuisance term \mathbf{V}_{ext} , namely the residual bulk flow, is introduced to encapsulate contributions from beyond the reconstruction volume D , and we treat it as a free parameter in our analysis. The Hubble recessional redshift z_h is given by [4, 8, 49]:

$$z_h = \frac{1}{1 + q_0} \left(1 - \sqrt{1 - \frac{2H_0 r}{c} (1 + q_0)} \right), \quad (5.4)$$

where the deceleration factor is given by $q_0 = \Omega_m/2 - \Omega_\Lambda$.

In observations, to accurately estimate the β parameter using the velocity-velocity comparison method, both the homogeneous and inhomogeneous Malmquist biases are required to be removed.

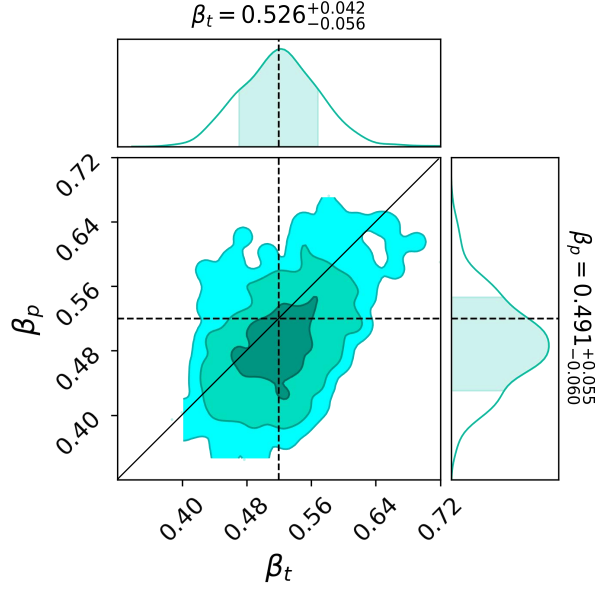


Figure 13. Comparison between the β measurements from the reconstructed velocity fields (β_p) and those from the true velocity fields (β_t) from the 538 testing sub-cubes. Top panel shows the probability distribution of β_t . Right side panel shows the probability distribution of β_p , the shade shows the 68% certainty (1σ) level. Black dashes indicate the fiducial value $\beta_{\text{fid}} = 0.52$. The 2D contours are the 68%, 95%, and 99.7% certainty levels. Solid line indicates the diagonal ($\beta_p = \beta_t$).

The homogeneous Malmquist bias is a consequence of selection effects, while the inhomogeneous Malmquist bias arises from local density variations due to large-scale structure along the line of sight [64, 66]. A commonly used method to remove these Malmquist biases is the Forward Likelihood estimation [51]. However, in this paper, we use simulations with the exact positions of the mock galaxies, and the Malmquist biases are negligible. Therefore, we use the simple χ^2 minimization to estimate β . The χ^2 between the predicted redshift and the observed redshift of galaxies is given by [4, 8]:

$$\chi^2(\beta, \mathbf{V}_{\text{ext}}) = \sum_{i=1}^{N_{\text{gal}}} \frac{(cz_{\text{obs},i} - cz_{p,i})^2}{\sigma_v^2}, \quad (5.5)$$

where z_{obs} is given by Eq. 2.6. The true galaxy peculiar velocities are used to compute z_{obs} , the measurement errors are zeros. Therefore, only the velocity dispersion σ_v appears in the above χ^2 . The parameters β and \mathbf{V}_{ext} are estimated by minimizing the above χ^2 .

In Fig. 13, we plot the estimations using the reconstructed velocity field, β_p , against the estimations from the true velocity field, β_t , from the 538 testing sub-cubes. The estimated β_p value ($\beta_p = 0.491^{+0.055}_{-0.060}$) agrees with the fiducial value 0.52 (dashed-lines) within the 68% confidence level, as shown in the shaded area in the right panel. However, the β_p estimated using the reconstructed velocity fields shows a systematic shift compared to the β_t , which is estimated from the true fields ($\beta_t = 0.526^{+0.042}_{-0.056}$). The scatters of β_p are result of the variance between the sub-cubes and the whole simulation box, as well as the variance between the V-net reconstructed fields and the true fields.

6 Conclusion

The peculiar velocities of galaxies serve as a valuable tool for studying the gravitational potential field, allowing for a more direct measurement of the large-scale distribution of matter than positions of galaxies alone. However, effectively utilizing these velocities requires a precise prediction of the density and velocity fields. In this study, we evaluate the effectiveness of a Convolutional Neural Network (CNN) architecture, the V-net, in reconstructing these fields and making inferences about the growth rate of cosmological structure.

In this work, the real-space density fields are reconstructed from input galaxy redshift catalogs using an initial V-net. Results indicate that tuning the loss function with density-dependent weights enhances the V-net’s accuracy in predicting density values across both low- and high-density regions. Additionally, the reconstructed density fields exhibit minimal contamination from redshift-space distortions in the input galaxy catalogs.

The velocity fields are then reconstructed from the density fields using another V-net. The results demonstrate that tuning the loss function with velocity-dependent weights enhances the accuracy of the V-net in predicting pixels with large velocity amplitudes. As with the reconstructed density fields, the velocity fields also exhibit reduced contamination from redshift-space distortions in the input galaxy catalogs.

The estimation of the cosmological parameter β through comparison of the reconstructed and true velocity fields yields results consistent with the fiducial value. While the β values estimated using the reconstructed velocity fields exhibit a systematic offset relative to the true fields, they still agree with the fiducial value within 1σ . This suggests that the density and velocity fields reconstructed using AI provide reasonably accurate constraints.

This study successfully illustrates the concept of reconstructing large-scale density and velocity fields through the use of a CNN architecture. However, its scope is limited, as it only considers a cubic geometry without observational selection effects, simplistic peculiar velocity errors, and only a single cosmological model. To address these complexities, additional simulations and training would be necessary, and such efforts are left for future studies.

Acknowledgments

FQ, DP, and SEH are supported by the project 우주거대구조를 이용한 암흑우주 연구 (“Understanding Dark Universe Using Large Scale Structure of the Universe”), funded by the Ministry of Science. CGS acknowledges support via the Basic Science Research Program from the National Research Foundation of South Korea (NRF) funded by the Ministry of Education (2018R1A6A1A06024977 and 2020R1I1A1A01073494). This work was supported by the high performance computing cluster Seondeok at the Korea Astronomy and Space Science Institute.

References

- [1] Basilakos, S., Plionis, M., & Ragone-Figueroa, C. 2008, ApJ, 678, 627, doi: [10.1086/586725](https://doi.org/10.1086/586725)
- [2] Berlind, A. A., Narayanan, V. K., & Weinberg, D. H. 2000, ApJ, 537, 537, doi: [10.1086/309085](https://doi.org/10.1086/309085)
- [3] Bilicki, M., & Chodorowski, M. J. 2008, MNRAS, 391, 1796, doi: [10.1111/j.1365-2966.2008.13988.x](https://doi.org/10.1111/j.1365-2966.2008.13988.x)
- [4] Boruah, S. S., Hudson, M. J., & Lavaux, G. 2020, MNRAS, 498, 2703, doi: [10.1093/mnras/staa2485](https://doi.org/10.1093/mnras/staa2485)
- [5] Branchini, E., Eldar, A., & Nusser, A. 2002, MNRAS, 335, 53, doi: [10.1046/j.1365-8711.2002.05611.x](https://doi.org/10.1046/j.1365-8711.2002.05611.x)

- [6] Branchini, E., Teodoro, L., Frenk, C. S., et al. 1999, MNRAS, 308, 1, doi: [10.1046/j.1365-8711.1999.02514.x](https://doi.org/10.1046/j.1365-8711.1999.02514.x)
- [7] Carleo, G., Cirac, I., Cranmer, K., et al. 2019, Reviews of Modern Physics, 91, 045002, doi: [10.1103/RevModPhys.91.045002](https://doi.org/10.1103/RevModPhys.91.045002)
- [8] Carrick, J., Turnbull, S. J., Lavaux, G., & Hudson, M. J. 2015, MNRAS, 450, 317, doi: [10.1093/mnras/stv547](https://doi.org/10.1093/mnras/stv547)
- [9] Chuang, C.-H., Zhao, C., Prada, F., et al. 2015, MNRAS, 452, 686, doi: [10.1093/mnras/stv1289](https://doi.org/10.1093/mnras/stv1289)
- [10] Colless, M., Saglia, R. P., Burstein, D., et al. 2001, MNRAS, 321, 277, doi: [10.1046/j.1365-8711.2001.04044.x](https://doi.org/10.1046/j.1365-8711.2001.04044.x)
- [11] Croft, R. A. C., & Gaztanaga, E. 1997, MNRAS, 285, 793, doi: [10.1093/mnras/285.4.793](https://doi.org/10.1093/mnras/285.4.793)
- [12] Davis, T. M., & Scrimgeour, M. I. 2014, MNRAS, 442, 1117, doi: [10.1093/mnras/stu920](https://doi.org/10.1093/mnras/stu920)
- [13] DESI Collaboration, Aghamousa, A., Aguilar, J., et al. 2016, arXiv e-prints, arXiv:1611.00036. <https://arxiv.org/abs/1611.00036>
- [14] Djorgovski, S., & Davis, M. 1987, ApJ, 313, 59, doi: [10.1086/164948](https://doi.org/10.1086/164948)
- [15] Erdoğdu, P., Lahav, O., Huchra, J. P., et al. 2006, MNRAS, 373, 45, doi: [10.1111/j.1365-2966.2006.11049.x](https://doi.org/10.1111/j.1365-2966.2006.11049.x)
- [16] Erdoğdu, P., Lahav, O., Huchra, J. P., et al. 2006, MNRAS, 373, 45, doi: [10.1111/j.1365-2966.2006.11049.x](https://doi.org/10.1111/j.1365-2966.2006.11049.x)
- [17] Ganeshaiah Veena, P., Lilow, R., & Nusser, A. 2022, arXiv e-prints, arXiv:2212.06439. <https://arxiv.org/abs/2212.06439>
- [18] Glorot, X., Bordes, A., & Bengio, Y. 2011, in ICML, 513–520. https://icml.cc/2011/papers/342_icmlpaper.pdf
- [19] He, S., Li, Y., Feng, Y., et al. 2019, Proceedings of the National Academy of Science, 116, 13825, doi: [10.1073/pnas.1821458116](https://doi.org/10.1073/pnas.1821458116)
- [20] Hinshaw, G., Larson, D., Komatsu, E., et al. 2013, ApJ, 208, 19, doi: [10.1088/0067-0049/208/2/19](https://doi.org/10.1088/0067-0049/208/2/19)
- [21] Hong, S. E., Jeong, D., Hwang, H. S., & Kim, J. 2021, ApJ, 913, 76, doi: [10.3847/1538-4357/abf040](https://doi.org/10.3847/1538-4357/abf040)
- [22] Hong, S. E., Kang, H., & Ryu, D. 2015, ApJ, 812, 49, doi: [10.1088/0004-637X/812/1/49](https://doi.org/10.1088/0004-637X/812/1/49)
- [23] Hong, S. E., Ryu, D., Kang, H., & Cen, R. 2014, ApJ, 785, 133, doi: [10.1088/0004-637X/785/2/133](https://doi.org/10.1088/0004-637X/785/2/133)
- [24] Hong, T., Staveley-Smith, L., Masters, K. L., et al. 2019, MNRAS, 1349, doi: [10.1093/mnras/stz1413](https://doi.org/10.1093/mnras/stz1413)
- [25] Howlett, C., Said, K., Lucey, J. R., et al. 2022, MNRAS, 515, 953, doi: [10.1093/mnras/stac1681](https://doi.org/10.1093/mnras/stac1681)
- [26] Huchra, J., Davis, M., Latham, D., & Tonry, J. 1983, ApJ, 52, 89, doi: [10.1086/190860](https://doi.org/10.1086/190860)
- [27] Hui, L., & Greene, P. B. 2006, Phys. Rev. D, 73, 123526, doi: [10.1103/PhysRevD.73.123526](https://doi.org/10.1103/PhysRevD.73.123526)
- [28] Ioffe, S., & Szegedy, C. 2015, in Proceedings of Machine Learning Research, Vol. 37, Proceedings of the 32nd International Conference on Machine Learning, ed. F. Bach & D. Blei (Lille, France: PMLR), 448–456. <https://proceedings.mlr.press/v37/ioffe15.html>
- [29] Ivezić, Ž., Kahn, S. M., Tyson, J. A., et al. 2008, arXiv e-prints, arXiv:0805.2366. <https://arxiv.org/abs/0805.2366>
- [30] Kingma, D. P., & Ba, J. 2014, arXiv e-prints, arXiv:1412.6980. <https://arxiv.org/abs/1412.6980>
- [31] Kitaura, F.-S., Angulo, R. E., Hoffman, Y., & Gottlöber, S. 2012, MNRAS, 425, 2422, doi: [10.1111/j.1365-2966.2012.21589.x](https://doi.org/10.1111/j.1365-2966.2012.21589.x)
- [32] Koribalski, B. S., Staveley-Smith, L., Westmeier, T., et al. 2020, Astrophysics and Space Science, 365, 118, doi: [10.1007/s10509-020-03831-4](https://doi.org/10.1007/s10509-020-03831-4)

- [33] Kudlicki, A., Chodorowski, M., Plewa, T., & Różyczka, M. 2000, MNRAS, 316, 464, doi: [10.1046/j.1365-8711.2000.03463.x](https://doi.org/10.1046/j.1365-8711.2000.03463.x)
- [34] Lilow, R., & Nusser, A. 2021, MNRAS, 507, 1557, doi: [10.1093/mnras/stab2009](https://doi.org/10.1093/mnras/stab2009)
- [35] Lucie-Smith, L., Peiris, H. V., Pontzen, A., & Lochner, M. 2018, MNRAS, 479, 3405, doi: [10.1093/mnras/sty1719](https://doi.org/10.1093/mnras/sty1719)
- [36] Ma, Y.-Z., Branchini, E., & Scott, D. 2012, MNRAS, 425, 2880, doi: [10.1111/j.1365-2966.2012.21671.x](https://doi.org/10.1111/j.1365-2966.2012.21671.x)
- [37] Mao, T.-X., Wang, J., Li, B., et al. 2021, MNRAS, 501, 1499, doi: [10.1093/mnras/staa3741](https://doi.org/10.1093/mnras/staa3741)
- [38] Merten, J., Giocoli, C., Baldi, M., et al. 2019, MNRAS, 487, 104, doi: [10.1093/mnras/stz972](https://doi.org/10.1093/mnras/stz972)
- [39] Milletari, F., Navab, N., & Ahmadi, S.-A. 2016, arXiv e-prints, arXiv:1606.04797, <https://arxiv.org/abs/1606.04797>
- [40] Modi, C., Feng, Y., & Seljak, U. 2018, J. Cosmol. Astropart. Phys., 2018, 028, doi: [10.1088/1475-7516/2018/10/028](https://doi.org/10.1088/1475-7516/2018/10/028)
- [41] Monaco, P. 2016, Galaxies, 4, 53, doi: [10.3390/galaxies4040053](https://doi.org/10.3390/galaxies4040053)
- [42] Monaco, P., Sefusatti, E., Borgani, S., et al. 2013, MNRAS, 433, 2389, doi: [10.1093/mnras/stt907](https://doi.org/10.1093/mnras/stt907)
- [43] Monaco, P., Theuns, T., & Taffoni, G. 2002, MNRAS, 331, 587, doi: [10.1046/j.1365-8711.2002.05162.x](https://doi.org/10.1046/j.1365-8711.2002.05162.x)
- [44] Monaco, P., Theuns, T., Taffoni, G., et al. 2002, ApJ, 564, 8, doi: [10.1086/324182](https://doi.org/10.1086/324182)
- [45] Munari, E., Monaco, P., Sefusatti, E., et al. 2017, MNRAS, 465, 4658, doi: [10.1093/mnras/stw3085](https://doi.org/10.1093/mnras/stw3085)
- [46] Ntampaka, M., Avestruz, C., Boada, S., et al. 2019, Bulletin of the American Astronomical Society, 51, 14. <https://arxiv.org/abs/1902.10159>
- [47] Nusser, A., Dekel, A., Bertschinger, E., & Blumenthal, G. R. 1991, ApJ, 379, 6, doi: [10.1086/170480](https://doi.org/10.1086/170480)
- [48] Pan, S., Liu, M., Forero-Romero, J., et al. 2020, Science China Physics, Mechanics, and Astronomy, 63, 110412, doi: [10.1007/s11433-020-1586-3](https://doi.org/10.1007/s11433-020-1586-3)
- [49] Peebles, P. 2020, in Principles of Physical Cosmology (Princeton University Press)
- [50] Percival, W., Balogh, M., Bond, D., et al. 2019, in Canadian Long Range Plan for Astronomy and Astrophysics White Papers, Vol. 2020, 20, doi: [10.5281/zenodo.3758532](https://doi.org/10.5281/zenodo.3758532)
- [51] Pike, R. W., & Hudson, M. J. 2005, ApJ, 635, 11, doi: [10.1086/497359](https://doi.org/10.1086/497359)
- [52] Qin, F. 2021, Research in Astronomy and Astrophysics, 21, 242, doi: [10.1088/1674-4527/21/10/242](https://doi.org/10.1088/1674-4527/21/10/242)
- [53] Qin, F., Howlett, C., & Staveley-Smith, L. 2019, MNRAS, 487, 5235, doi: [10.1093/mnras/stz1576](https://doi.org/10.1093/mnras/stz1576)
- [54] Qin, F., Howlett, C., Stevens, A. R. H., & Parkinson, D. 2022, ApJ, 937, 113, doi: [10.3847/1538-4357/ac8b6f](https://doi.org/10.3847/1538-4357/ac8b6f)
- [55] Qin, F., Parkinson, D., Howlett, C., & Said, K. 2021, ApJ, 922, 59, doi: [10.3847/1538-4357/ac249d](https://doi.org/10.3847/1538-4357/ac249d)
- [56] Ravanbakhsh, S., Oliva, J., Fromenteau, S., et al. 2017, arXiv e-prints, arXiv:1711.02033, <https://arxiv.org/abs/1711.02033>
- [57] Rizzo, L. A., Villaescusa-Navarro, F., Monaco, P., et al. 2017, J. Cosmol. Astropart. Phys., 2017, 008, doi: [10.1088/1475-7516/2017/01/008](https://doi.org/10.1088/1475-7516/2017/01/008)
- [58] Ronneberger, O., Fischer, P., & Brox, T. 2015, arXiv e-prints, arXiv:1505.04597, <https://arxiv.org/abs/1505.04597>
- [59] Said, K., Colless, M., Magoulas, C., Lucey, J. R., & Hudson, M. J. 2020, MNRAS, 497, 1275, doi: [10.1093/mnras/staa2032](https://doi.org/10.1093/mnras/staa2032)

- [60] Scrimgeour, M. I., Davis, T. M., Blake, C., et al. 2016, MNRAS, 455, 386, doi: [10.1093/mnras/stv2146](https://doi.org/10.1093/mnras/stv2146)
- [61] Springel, V. 2005, MNRAS, 364, 1105, doi: [10.1111/j.1365-2966.2005.09655.x](https://doi.org/10.1111/j.1365-2966.2005.09655.x)
- [62] Springel, V., Yoshida, N., & White, S. D. M. 2001, New Astronomy, 6, 79, doi: [10.1016/S1384-1076\(01\)00042-2](https://doi.org/10.1016/S1384-1076(01)00042-2)
- [63] Springob, C. M., Magoulas, C., Colless, M., et al. 2014, MNRAS, 445, 2677, doi: [10.1093/mnras/stu1743](https://doi.org/10.1093/mnras/stu1743)
- [64] Springob, C. M., Hong, T., Staveley-Smith, L., et al. 2016, MNRAS, 456, 1886, doi: [10.1093/mnras/stv2648](https://doi.org/10.1093/mnras/stv2648)
- [65] Square Kilometre Array Cosmology Science Working Group, Bacon, D. J., Battye, R. A., et al. 2020, PASA, 37, e007, doi: [10.1017/pasa.2019.51](https://doi.org/10.1017/pasa.2019.51)
- [66] Strauss, M. A., & Willick, J. A. 1995, ApJ, 261, 271, doi: [10.1016/0370-1573\(95\)00013-7](https://doi.org/10.1016/0370-1573(95)00013-7)
- [67] Taffoni, G., Monaco, P., & Theuns, T. 2002, MNRAS, 333, 623, doi: [10.1046/j.1365-8711.2002.05441.x](https://doi.org/10.1046/j.1365-8711.2002.05441.x)
- [68] Tinker, J. L., Weinberg, D. H., Zheng, Z., & Zehavi, I. 2005, ApJ, 631, 41, doi: [10.1086/432084](https://doi.org/10.1086/432084)
- [69] Tully, R. B., & Fisher, J. R. 1977, A&A, 54, 661
- [70] Wang, H., Mo, H. J., Yang, X., & van den Bosch, F. C. 2012, MNRAS, 420, 1809, doi: [10.1111/j.1365-2966.2011.20174.x](https://doi.org/10.1111/j.1365-2966.2011.20174.x)
- [71] Wu, Z., Zhang, Z., Pan, S., et al. 2021, ApJ, 913, 2, doi: [10.3847/1538-4357/abf3bb](https://doi.org/10.3847/1538-4357/abf3bb)
- [72] Zaroubi, S., Hoffman, Y., Fisher, K. B., & Lahav, O. 1995, ApJ, 449, 446, doi: [10.1086/176070](https://doi.org/10.1086/176070)
- [73] Zhang, X., Wang, Y., Zhang, W., et al. 2019, arXiv e-prints, arXiv:1902.05965. <https://arxiv.org/abs/1902.05965>